Effect of humidity of reactants on the cell performance of PEM fuel cells with parallel and interdigitated flow field designs

Xiao-Dong Wang [a], Yuan-Yuan Duan [b], Wei-Mon Yan [c,*], Fang-Bor Weng [d]

[a] *Department of Thermal Engineering, School of Mechanical Engineering, University of Science & Technology Beijing, Beijing 100083, China*
[b] *Key Laboratory for Thermal Science and Power Engineering of Ministry of Education, Tsinghua University, Beijing 100084, China*
[c] *Department of Mechatronic Engineering, Huafan University, Taipei 22305, Taiwan*
[d] *Department of Mechanical Engineering, Yuan Ze University, Tao Yuan 320, Taiwan*

Abstract

This study investigates the effects of the relative humidity (RH) of the reactants on the cell performance and local transport phenomena in proton exchange membrane fuel cells with parallel and interdigitated flow fields. A three-dimensional model was developed taking into account the effect of the liquid water formation on the reactant transport. The results indicate that the reactant RH and the flow field design all significantly affect cell performance. For the same operating conditions and reactant RH, the interdigitated design has better cell performance than the parallel design. With a constant anode RH = 100%, for lower operating voltages, a lower cathode RH reduces cathode flooding and improves cell performance, while for higher operating voltages, a higher cathode RH maintains the membrane hydration to give better cell performance. With a constant cathode RH = 100%, for lower operating voltages, a lower anode RH not only provides more hydrogen to the catalyst layer to participate in the electrochemical reaction, but also increases the difference in the water concentrations between the anode and cathode, which enhances back-diffusion of water from the cathode to the anode, thus reducing cathode flooding to give better performance. However, for higher operating voltages, the cell performance is not dependent on the anode RH.
© 2007 Elsevier B.V. All rights reserved.

Keywords: Modeling; Flow field design; Humidity; Proton exchange membrane fuel cell

1. Introduction

Fuel cells have attracted much attention in recent years as a promising alternative to traditional internal combustion engines due to their high power density and ultra-low emissions. Of the various types of fuel cells, the proton exchange membrane fuel cell (PEMFCs) operates at near-room temperatures and is considered to be a good choice for automotive applications [1–3].

Water management is critical to the PEMFC performance. It is well known that the currently used commercial polymer electrolyte membrane (PEM) in PEMFCs must be well hydrated to maintain high-proton conductivity, which is proportional to the water content of the polymer membrane. Decreasing water content in the polymer membrane leads to reduced performance due to increases of the voltage loss in the membrane. To avoid dehydration of the polymer electrolyte, the inlet flows are usually injected with water vapor. In addition, the electrochemical reactions at the cathode produce water vapor, which may condense and accumulate in the pores of the porous medium and water is also transported from the anode to the cathode due to electro-osmosis. Excessive liquid water can cause flooding of the pores in the catalyst layers (CL) and the gas diffusion layers (GDL), thus increasing the higher mass transfer resistance to the reactant flow. Generally, proper flow field design in the bipolar plates is an effective means to prevent cathode flooding and increase reactant transport.

Numerous studies have presented theoretical models to describe the water transport in PEMFCs [4–29]. The earliest and most cited models were developed by Springer et al. [4] and Bernardi and Vebrugge [5,6]. Springer et al. [4] presented

* Corresponding author. Tel.: +886 2 2663 2102; fax: +886 2 2663 1119.
E-mail address: wmyan@huafan.hfu.edu.tw (W.-M. Yan).

Nomenclature

a	chemical activity of water vapor
$Aj_{0,a}^{ref}$	exchange current density at anode (A m^{-3})
$Aj_{0,c}^{ref}$	exchange current density at cathode (A m^{-3})
b	source term of variable ϕ
C	mass fraction
C_F	quadratic drag factor
d_{porous}	equivalent surface diameter of porous media (m)
D	mass diffusivity (m^2 s^{-1})
F	Faraday constant (96,487 C mol^{-1})
i	current density (A m^{-2})
I	average current density in the fuel cell (A m^{-2})
I_y	local current density in the y direction (A m^{-2})
j	current density (A m^{-3})
k_c	water vapor condensation rate coefficient (s^{-1})
k_e	water vapor evaporation rate coefficient (s^{-1})
k_p	permeability (m^2)
M	molecular weight (kg mol^{-1})
P	pressure (atm)
P'	perturbed pressure in a control volume
R	universal gas constant (8.314 J mol^{-1} K^{-1})
s	volume ratio occupied by liquid water
S_c	corrected source term in the concentration equation
S_j	source term in the phase potential equation
S_L	source term accounting for the liquid water effect
S_u	source term in the x momentum equation
S_v	source term in the y momentum equation
S_w	source term in the z momentum equation
S'	surface area (m^2)
t	time (s)
T	temperature (K)
u	x direction velocity (m s^{-1})
v	y direction velocity (m s^{-1})
V_{cell}	operating voltage (V)
V'	volume (m^3)
w	z direction velocity (m s^{-1})
x	x direction coordinate (m)
y	y direction coordinate (m)
z	z direction coordinates (m)
Z_f	species valence

Greek letters

α_a	electrical transfer coefficient in the forward reaction
α_c	electrical transfer coefficient in the backward reaction
ε	porosity
ϕ	dependent variables
Φ	phase potential function
η	overpotential (V)
λ	membrane water content
ν	kinematic viscosity (m^2 s^{-1})
ρ	density (kg m^{-3})

σ_m	membrane electrical conductivity
τ	tortuosity of the pores in the porous medium
$\varXi_\phi$	exchange coefficient

subscripts

a	anode
c	cathode
channel	channel
CL	catalyst layer
eff	effective
GDL	gas diffusion layer
H$^+$	hydrogen ion
H$_2$	hydrogen
H$_2$O	water
k	kth component of the mixture
MEM	membrane
O$_2$	oxygen
porous	porous medium
sat	saturation
total	total
x	x direction
y	y direction
z	z direction

superscripts

ref	reference value

a one-dimensional steady-state model for a PEMFC, in which water diffusion coefficients, electro-osmotic drag coefficient, water sorption isotherms, and membrane conductivity were measured as a function of the membrane water content. With the assumption of a fully hydrated membrane, Bernardi and Verbrugge [5] derived a mathematical model for the cathode side of a PEMFC and found that the water transport is a complicated function of the cell operating conditions. They further presented a full cell model [6] to investigate the water transport mechanisms.

Other important early fuel cell models included those by Fuller and Newman [7] and Nguyen and White [8]. Fuller and Newman [7] presented a quasi-two-dimensional, along-the-channel model with the assumption of a constant water diffusivity in the membrane to examine the water management problems in a PEMFC. Nguyen and White [8] also developed a steady-state, two-dimensional model, including the effect of electro-osmosis, water diffusion, and heat transfer from the solid phase to the gas phase and the latent heat due to water evaporation and condensation, to investigate the effectiveness of various humidification designs. Okada et al. [9] studied the water transport on the anode side and gave a linear transport equation based on the water diffusion and electro-osmotic water drag to analyze the water concentration profiles. Their results showed that the water concentration profile is influenced by the membrane thickness and humidity and the current density in the cell. Gurau et al. [10] considered the variations of the concentrations and partial pressures in the gas channels in a two-dimensional model

for the entire PEMFC sandwich. They further derived a half-cell model for the cathode side and obtained rigorous analytical solutions which account for the liquid water content in the GDL [11].

Yi and Nguyen [12] developed an along-the-channel model to evaluate the effects of various design and operating parameters on the performance of PEMFCs to show that humidification of the anode reactants is required to enhance the membrane conductivity and liquid injection and higher humidification temperatures can improve cell performance by introducing more water into the anode. Hsing and Futerko [13] developed a two-dimensional model coupling the fluid flow, mass transport and electrochemistry of a PEMFC taking into account the variation of the liquid water diffusion coefficient in the membrane. Baschuk and Li [14] considered the effect of variable degrees of flooding on the cathode and presented a model to evaluate its influence on cell performance. Um et al. [15] presented a transient multidimensional model to simulate multi-component transport in a PEMFC and explored hydrogen dilution effects in the anode feed. Djilali and Lu [16] focused on the modeling of non-isothermal and non-isobaric effects and performed an analysis of the cell performance and water transport over a range of operating current densities. Kulikovsky [17] used a quasi-three-dimensional model of the water transport in PEMFCs to investigate the non-linear diffusion of liquid water in the membrane. Ge and Yi [18] developed a two-dimensional model to investigate the effects of operating conditions and membrane thickness on the water transport. They used an effective porosity to account for the effect of liquid water on the gas transport to simplify the two-phase flow model in the porous layers. Siegel et al. [19] derived a comprehensive two-dimensional model that included multi-component and multi-phase transport both along the gas channel and through the membrane electrode assembly (MEA). Their results illustrated the importance of water transport within the cell. Mazumder and Cole [20,21] developed a three-dimensional model to predict the effect of the formation of liquid water on the performance of PEMFCs. Yan and co-workers [22–32] developed two-dimensional and three-dimensional models for the reactants and water transport and the cell performance in PEMFCs with various flow field designs. The effects of liquid water formation on the reactant transport were taken into account in the modeling and examined in the analysis. Recently, Wang [33] reviewed the fundamental models for PEMFCs.

The membrane stability is determined by its water content. Proper hydration of the membrane is critical for maintaining membrane conductivity and mechanical stability. Various humidification designs such as internal humidification, external humidification and direct injection methods are used in PEMFCs to maintain hydration of the polymer membrane [8,34–41]. Recently, Jang et al. [42] developed a two-dimensional model to investigate the effect of the humidity of the reactants at the inlet on the detailed gas transport and cell performance of the PEMFC with baffle-blocked flow field designs. Lee and Chu [43] used a three-dimensional model to investigate the location of the gas–liquid interface for various cathode humidity conditions in the cathode gas diffusion layer for the conventional flow field. In their study, only part of the cell was simulated to reduce the computational effort. These studies revealed that the relative humidity (RH) critically affects cell performance.

These results have shown that the optimal cell performance is strongly dependent on the water management. Proper humidification of the reactants can improve membrane hydration and an appropriate flow field design in the bipolar plates can increase reactant transport and liquid water removal. Though some studies have analyzed the effect of the relative humidity of the reactants on the PEMFC performance, most previous investigations have utilized simplified two-dimensional models or only considered some essential parts of the fuel cell in the computational domain to reduce the computational time. This paper presents a three-dimensional, full cell model to investigate the effects of the relative humidity of the reactants on both the anode and cathode sides on the cell performance for PEMFCs with parallel and interdigitated flow fields. The effects of liquid water formation on the reactant transport are taken into account in the model. The local oxygen/hydrogen mass flow rates, liquid water distributions, and local current densities in the cell for both flow fields are examined to validate the simulation results.

2. Analysis

A three-dimensional model of the full cell was developed to analyze the electrochemical reactions and transport phenomena of the reactants and products in the cell. The cell was divided into the anode flow channels, membrane electrode assembly (including the anode GDL, anode CL, proton exchange membrane, cathode CL, and cathode GDL), and cathode flow channels as shown in Fig. 1. The governing equations include the mass, momentum, species and electrical potential conservation equations. The model assumes that the system is three-dimensional and steady; the inlet fuels are ideal gases; the system is isothermal; the flow is laminar; the fluid is incompressible; the thermal properties are constant; the porous layers including the gas diffusion layer, catalyst layer and PEM, are isotropic. The present model is based on the so-called multiphase multicomponent mixture, originally proposed by Wang et al. The transport equations for the three-dimensional PEM fuel cell are:
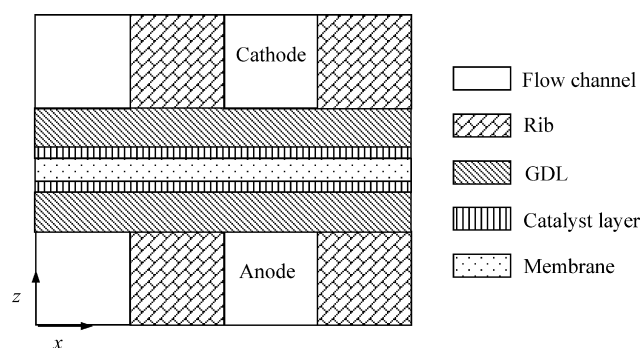

Fig. 1. Schematic of the cross-section of a PEMFC (not to scale and with only two channels and two ribs shown).

Table 1
Source terms in the governing equations

	S_u	S_v	S_w	S_c
Channel	0	0	0	–
GDL	$-\dfrac{v\varepsilon_{\text{eff}}^2}{k_p}u - \dfrac{\varepsilon_{\text{eff}}^3 C_F\rho u}{\sqrt{k_p}}\sqrt{u^2+v^2+w^2}$	$-\dfrac{v\varepsilon_{\text{eff}}^2}{k_p}v - \dfrac{\varepsilon_{\text{eff}}^3 C_F\rho v}{\sqrt{k_p}}\sqrt{u^2+v^2+w^2}$	$-\dfrac{v\varepsilon_{\text{eff}}^2}{k_p}w - \dfrac{\varepsilon_{\text{eff}}^3 C_F\rho w}{\sqrt{k_p}}\sqrt{u^2+v^2+w^2}$	0
Catalyst layer	$-\dfrac{v\varepsilon_{\text{eff}}^2}{k_p}u - \dfrac{\varepsilon_{\text{eff}}^3 C_F\rho u}{\sqrt{k_p}}\sqrt{u^2+v^2+w^2}$	$-\dfrac{v\varepsilon_{\text{eff}}^2}{k_p}v - \dfrac{\varepsilon_{\text{eff}}^3 C_F\rho v}{\sqrt{k_p}}\sqrt{u^2+v^2+w^2}$	$-\dfrac{v\varepsilon_{\text{eff}}^2}{k_p}w - \dfrac{\varepsilon_{\text{eff}}^3 C_F\rho w}{\sqrt{k_p}}\sqrt{u^2+v^2+w^2}$	$H_2: -\dfrac{1}{2FC_{\text{total,a}}}\cdot j_a$; $O_2: -\dfrac{1}{4FC_{\text{total,c}}}\cdot j_c$; $H_2O: \dfrac{1}{2FC_{\text{total,c}}}\cdot j_c$
Membrane	$-\dfrac{v\varepsilon_{\text{eff}}^2}{k_p}u - \dfrac{\varepsilon_{\text{eff}}^3 C_F\rho u}{\sqrt{k_p}}\sqrt{u^2+v^2+w^2} + \dfrac{k_p}{v}Z_f C_{H^+}F\cdot\nabla\Phi\cdot u_x$	$-\dfrac{v\varepsilon_{\text{eff}}^2}{k_p}v - \dfrac{\varepsilon_{\text{eff}}^3 C_F\rho v}{\sqrt{k_p}}\sqrt{u^2+v^2+w^2} + \dfrac{k_p}{v}Z_f C_{H^+}F\cdot\nabla\Phi\cdot v_y$	$-\dfrac{v\varepsilon_{\text{eff}}^2}{k_p}w - \dfrac{\varepsilon_{\text{eff}}^3 C_F\rho w}{\sqrt{k_p}}\sqrt{u^2+v^2+w^2} + \dfrac{k_p}{v}Z_f C_{H^+}F\cdot\nabla\Phi\cdot w_z$	$\dfrac{Z_f F}{RT}D_{k,\text{eff},H^+}C_{H^+}\left(\dfrac{\partial^2\Phi}{\partial x^2}+\dfrac{\partial^2\Phi}{\partial y^2}+\dfrac{\partial^2\Phi}{\partial z^2}\right)$

- Continuity equation:

$$\frac{\partial u}{\partial x} + \frac{\partial v}{\partial y} + \frac{\partial w}{\partial z} = 0 \tag{1}$$

- x momentum equation:

$$\varepsilon_{\text{eff}}\left(u\frac{\partial u}{\partial x} + v\frac{\partial u}{\partial y} + w\frac{\partial u}{\partial z}\right) = -\frac{\varepsilon_{\text{eff}}}{\rho}\frac{\partial P}{\partial x} + v\varepsilon_{\text{eff}}\left(\frac{\partial^2 u}{\partial x^2} + \frac{\partial^2 u}{\partial y^2} + \frac{\partial^2 u}{\partial z^2}\right) + S_u \tag{2}$$

- y momentum equation:

$$\varepsilon_{\text{eff}}\left(u\frac{\partial v}{\partial x} + v\frac{\partial v}{\partial y} + w\frac{\partial v}{\partial z}\right) = -\frac{\varepsilon_{\text{eff}}}{\rho}\frac{\partial P}{\partial y} + v\varepsilon_{\text{eff}}\left(\frac{\partial^2 v}{\partial x^2} + \frac{\partial^2 v}{\partial y^2} + \frac{\partial^2 v}{\partial z^2}\right) + S_v \tag{3}$$

- z momentum equation:

$$\varepsilon_{\text{eff}}\left(u\frac{\partial w}{\partial x} + v\frac{\partial w}{\partial y} + w\frac{\partial w}{\partial z}\right) = -\frac{\varepsilon_{\text{eff}}}{\rho}\frac{\partial P}{\partial z} + v\varepsilon_{\text{eff}}\left(\frac{\partial^2 w}{\partial x^2} + \frac{\partial^2 w}{\partial y^2} + \frac{\partial^2 w}{\partial z^2}\right) + S_w \tag{4}$$

In the momentum equations, S_u, S_v and S_w are the source terms based on the Darcy drag forces in the x, y, and z directions imposed by the pore walls on the fluid which usually cause significant pressure drops across the porous media. The details of S_u, S_v and S_w for the various layers are listed in Table 1. In Table 1, ε_{eff} is the effective porosity of the porous material, C_F is the quadratic drag factor, and Z_f is the ion valence in the PEM. In addition, $D_{k,\text{eff}}$ is the effective diffusion coefficient of the kth species, which was calculated using the Bruggeman equation [44], and k_p are the permeabilities of the porous materials. The relationship between the porosity and the permeability was described by the Blake–Kozeny equation [45]:

$$k_p = \left(\frac{d_{\text{porous}}^2}{150}\right)\left[\frac{\varepsilon^3}{(1-\varepsilon)^2}\right] \tag{5}$$

where d_{porous} is the equivalent pore diameter of the porous material expressed as $d_{\text{porous}} = 6V'_{\text{porous}}/S'_{\text{porous}}$:

- Species concentration equation:

$$\varepsilon_{\text{eff}}\left(u\frac{\partial C_k}{\partial x} + v\frac{\partial C_k}{\partial y} + w\frac{\partial C_k}{\partial z}\right) = D_{k,\text{eff}}\left(\frac{\partial^2 C_k}{\partial x^2} + \frac{\partial^2 C_k}{\partial y^2} + \frac{\partial^2 C_k}{\partial z^2}\right) + S_c + S_L \tag{6}$$

where C_k is the concentration of the kth component and S_c and S_L are the source terms for the chemical reaction and the liquid water in the species concentration equation. S_c differs for the various reactant gases, e.g. S_c is $-j_a/2FC_{\text{total,a}}$ for hydrogen, $-j_c/4FC_{\text{total,c}}$ for oxygen, and $j_c/2FC_{\text{total,c}}$ for water vapor. The parameters j_a and j_c denote the current densities on the anode and

cathode sides, which can be calculated using the Butler–Volmer equations [10]:

$$j_a = A j_{0,a}^{ref} \left(\frac{C_{H_2}}{C_{H_2}^{ref}} \right) \left[e^{(\alpha_a F/RT)\eta} - \frac{1}{e^{(\alpha_c F/RT)\eta}} \right] \qquad (7)$$

$$j_c = A j_{0,c}^{ref} \left(\frac{C_{O_2}}{C_{O_2}^{ref}} \right) \left[e^{(\alpha_a F/RT)\eta} - \frac{1}{e^{(\alpha_c F/RT)\eta}} \right] \qquad (8)$$

where $A j_0^{ref}$ is the reference exchange current density, α_a and α_c are the electrical charge transport rates in the anode and cathode catalyst layers, η the overpotential, F the Faraday's constant, R the ideal gas constant and T is the fuel cell temperature. The local current density distribution was calculated from the phase potential equation:

$$\frac{\partial}{\partial x}\left(\sigma_m \frac{\partial \Phi}{\partial x}\right) + \frac{\partial}{\partial y}\left(\sigma_m \frac{\partial \Phi}{\partial y}\right) + \frac{\partial}{\partial z}\left(\sigma_m \frac{\partial \Phi}{\partial z}\right) = S_j \qquad (9)$$

where Φ is the phase potential and σ_m is the membrane conductivity which is strongly dependent on the membrane water content and can be calculated using the formulas developed by Springer [4]:

$$\sigma_m(T) = \sigma_m^{ref} \exp\left[1268\left(\frac{1}{303} - \frac{1}{T}\right)\right] \qquad (10)$$

where σ_m^{ref} is the membrane reference conductivity expressed as

$$\sigma_m^{ref} = 0.005139\lambda - 0.00326 \qquad (11)$$

$$\lambda = \begin{cases} 0.043 + 17.81a - 39.85a^2 + 36.0a^3, & 0 \le a \le 1 \\ 14 + 1.4(a-1), & 1 < a \le 3 \end{cases} \qquad (12)$$

where a is the water activity given by $a = C_{H_2O} RT / P_{sat}$, and λ is the water content in the PEM. S_j in Eq. (9) is the electrical source term, which is zero in the PEM without electrochemical reactions and is $-j_a$ or $-j_c$ on the anode or cathode sides. The current density, i, is related to the phase potential, Φ, as

$$i_x = -\sigma_m \frac{\partial \Phi}{\partial x} \qquad (13)$$

$$i_y = -\sigma_m \frac{\partial \Phi}{\partial y} \qquad (14)$$

$$i_z = -\sigma_m \frac{\partial \Phi}{\partial z} \qquad (15)$$

Eq. (9) can then be rewritten as

$$\frac{\partial i_x}{\partial x} + \frac{\partial i_y}{\partial y} + \frac{\partial i_z}{\partial z} = S_j \qquad (16)$$

During cell operation, the partial pressure of the water in the electrode may exceed its saturation pressure if the local water concentration is high. Therefore, when the water vapor partial pressure was greater than the water vapor saturation pressure, the water vapor was assumed to condense and fill the pores in the porous media. Operating the cell at high reaction rates may cause severe mass transport overpotential because the diffusing components are blocked. Furthermore, the extremely small pores in

the porous media cause capillary forces to dominate the liquid water transport. However, the actual expression of this force cannot be formulated. To simplify the complex two-phase flow, the simplified liquid water transport equation, originally proposed by Mazumder et al. [21], was used in the present model. In addition, the liquid water formation will affect the effective porosity and the mass diffusivity in the gas diffusion and catalyst layers. This approach was also adopted by Nguyen et al. [44]. The source term, S_L, in the species concentration equation, which is a function of the liquid water saturation, was evaluated as [21]

$$S_L = \begin{cases} -M_{H_2O}k_c \dfrac{\varepsilon_{eff}C_{H_2O}}{\rho RT}(P_{H_2O} - P_{sat}), & \text{if } P_{H_2O} > P_{sat} \\ k_e \varepsilon_{eff} s(P_{sat} - P_{H_2O}), & \text{if } P_{H_2O} < P_{sat} \end{cases} \qquad (17)$$

where the saturation rate, s, was defined as the ratio of the pore volume occupied by liquid water to the total pore volume in the porous media, M the molecular weight, k_c and k_e are the vapor condensation and evaporation rate coefficients, and P_{sat} is the water vapor saturation pressure calculated using [25,26,39]:

$$P_{sat} = 10^{-2.1794+0.02953T-9.1837\times10^{-5}T^2+1.4454\times10^{-7}T^3} \qquad (18)$$

The effective porosity of the porous media was then modified to account for the liquid water:

$$\varepsilon_{eff} = \varepsilon(1-s) \qquad (19)$$

Eqs. (1)–(4), (6) and (16) form a complete set of governing equations for the PEMFC. The boundary conditions at the anode flow channels and the cathode flow channels are that the inlet flow rates are constant, the inlet gas compositions are constant, and the flows are fully developed at the anode and cathode flow channels outlets. The solid walls are no slip with zero flux boundary conditions. At the interfaces between the gas channels, the diffusion layers, the catalyst layers, and the PEM, the velocities, mass fractions, momentum fluxes, and mass fluxes are assumed equal. More details were given by Yan and co-workers [26].

3. Numerical method

The SIMPLE (semi implicit method for pressure-linked equation) algorithm, developed by Patankar [46], was employed to solve the governing equations. The cell performance was simulated for a miniature cell with dimensions of $x \times y \times z = 23\,mm \times 23\,mm \times 2.845\,mm$. The cell had 12 channels (6 inlet flow channels and 6 outlet flow channels for the interdigitated flow channel design) and 11 ribs, all 1 mm thick. The diffusion layer was 0.4 mm thick, the catalyst layer was 0.005 mm thick, and the PEM was 0.035 mm thick as shown in Fig. 2. The anode flow channels were assumed to be in parallel with 1 mm channel and rib widths since the anode flow channel has little effect on the cell performance, while the cathode flow channels were assumed to be parallel or interdigitated flow channels with 1 mm channel and rib widths. The base operating conditions for the fuel cell were assumed to be a fuel cell temperature of 323 K, the reactant gases on the anode side were hydrogen and water vapor with a relative humidity of 100%, the

(a)

Section A
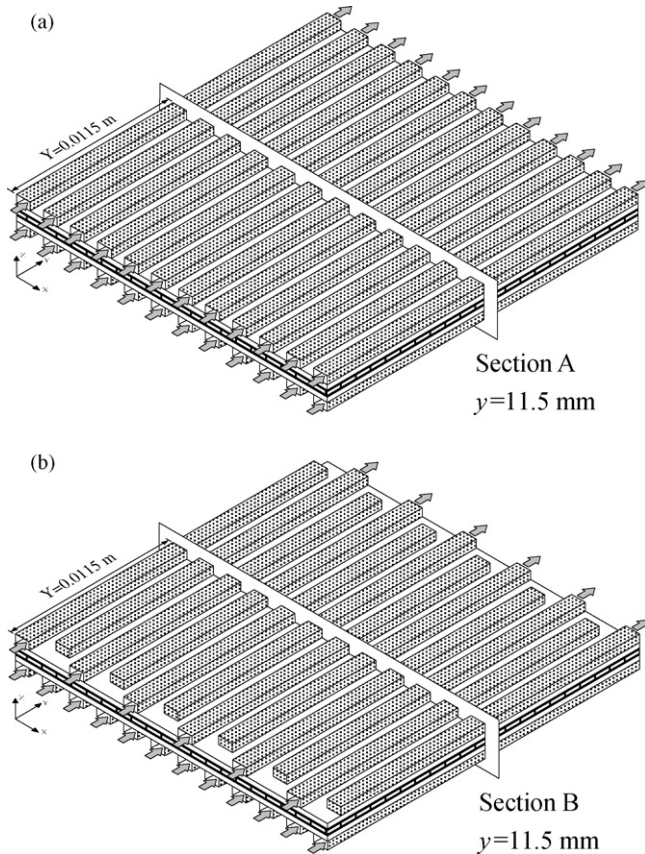$y = 11.5$ mm

(b)

Section B
$y = 11.5$ mm

Fig. 2. Schematic of PEMFC designs: (a) parallel flow field; (b) interdigitated flow field.

reactant gases on the cathode side contained oxygen, nitrogen, and water vapor with a relative humidity of 100%, the inlet flow rate on the anode side was 260 cc min^{-1}, the inlet flow rate on the cathode side was 700 cc min^{-1}, and the inlet pressures on the anode and cathode sides were both 1 atm. All of the fixed parameters used in the model are listed in Table 2. To study the effect of the relative humidity on the cathode side, RH$_c$ was chosen as 25%, 50%, 75%, and 100% with a constant RH$_a$ = 100%.

Table 2
Fuel cell parameters

Parameter	Value
$A j_{0,a}^{ref}$	9×10^8 A m^{-3}
$A j_{0,c}^{ref}$	1.5×10^2 A m^{-3}
α_a	0.5
α_c	1.5
$\varepsilon_{channel}$	1
$\tau_{channel}$	1
$k_{channel}$	∞ m^2
ε_{GDL}	0.5
τ_{GDL}	1.5
k_{GDL}	1.76×10^{-10} m^2
ε_{CL}	0.4
τ_{CL}	1.5
k_{CL}	1.76×10^{-11} m^2
ε_{Mem}	0.28
τ_{Mem}	Dagan Model
k_{Mem}	1.8×10^{-18} m^2

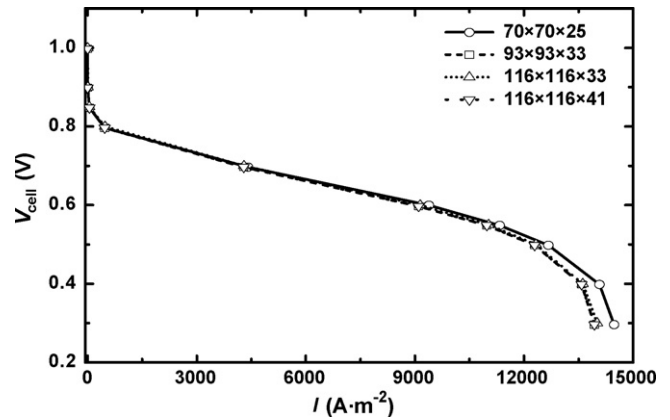Fig. 3. Influence of the number of elements on the polarization curves.

Similarly, RH$_a$ was chosen as 25%, 50%, 75%, and 100% with a constant RH$_c$ = 100% to analyze the effect of the RH$_a$.

The grid independence was examined in preliminary test runs. Four non-uniformly distributed grid configurations were evaluated for the parallel flow channel design with the numbers of elements in the x, y and z directions being: (I) $70 \times 70 \times 25$, (II) $93 \times 93 \times 33$, (III) $116 \times 116 \times 33$, and (IV) $116 \times 116 \times 41$. The influence of the number of elements on the polarization curves (I–V_{cell} curves) for the fuel cell is shown in Fig. 3. Grid (III) was chosen for the simulations as a tradeoff between accuracy and execution time. The coupled set of equations was solved iteratively and the solution was considered to be converged when the relative error in each field between two consecutive iterations was less than 10^{-6}.

The numerical results were validated by comparing the present predictions with previous experimental results. Fig. 4 compares the calculated polarization curve with experimental data [47] for a fuel cell with the parallel flow channel design and an area of 140 mm × 140 mm. There is only a small difference between the numerical results and the experimental data. Hence, the three-dimensional numerical model can be used to accurately analyze the effects of the flow channel area ratio and cathode fuel flow rate on the cell performance.
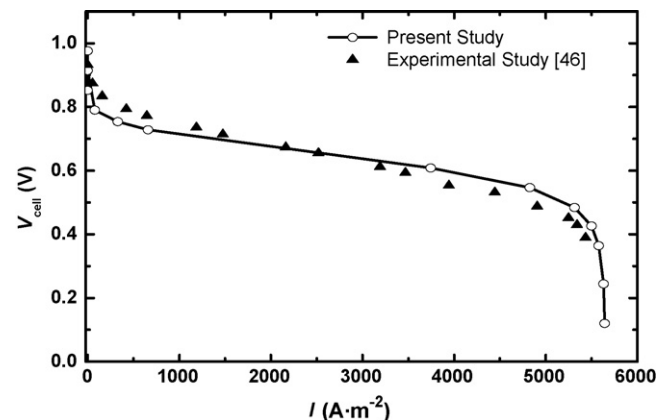

Fig. 4. Comparison of predicted and measured polarization curves for a fuel cell with the parallel flow channel design.

4. Results and discussion

The PEMFC performance is strongly dependent on the water management in the cell which includes two aspects. First, the membrane hydration must be maintained for proton transport, since the ohmic resistance of the membrane increases as the membrane water content decreases, which reduces cell performance. Secondly, the electrochemical reaction on the cathode side produces water vapor and when the partial pressure of the water vapor is higher than its saturation pressure, the water vapor condenses to form liquid water. In addition, water is also transported from the anode to the cathode by electro-osmotic drag. When the water generation rate on the cathode side by electro-osmotic drag and the oxygen reduction reaction exceeds the water removal rate from the cathode by back-diffusion to the anode, evaporation, and capillary transport of liquid water through the cathode gas diffusion layer and catalyst layer, the cathode becomes flooded. Excessive accumulated liquid water blocks the gas pores in the diffusion layer and the catalyst layer, which forms a barrier over the catalyst active surface in the catalyst layer, worsening the performance. In general, humidification of the reactants can ensure membrane hydration, but may induce cathode flooding. Proper flow field design is considered to be an effective means to prevent cathode flooding because it can increase reactant transport rates and enhance liquid water removal. This discussion analyzes the effects of the relative humidity of the reactants on both the cathode and anode sides on the cell performance for parallel and interdigitated flow fields.

4.1. Effect of cathode relative humidity

Fig. 5(a) and (b) show the $I–V_{cell}$ polarization curves for parallel and interdigitated flow fields for various cathode relative humidities with a constant $RH_a = 100\%$. At low-operating voltages for both flow fields, the cell performance decreases as RH_c increases. The cell performance is the best for $RH_c = 25\%$ and the worst for $RH_c = 100\%$ because at low-operating voltages, the electrochemical reactions are stronger with more liquid water produced on the cathode side, so the back-diffusion of water and the high anode relative humidity, $RH_a = 100\%$, provide sufficient water for the membrane. Thus, the cell performance is mainly dependent on the cathode mass transport limitations due to the liquid water blockage effect. When RH_c is lower, the oxygen concentration in the reactants is higher and the water vapor concentration on the cathode side is lower, which reduces the cathode flooding, so the cell performance increases. However, as the operating voltage increases, the effect of RH_c on the cell performance reverses (this operating voltage is referred to here as the reversal operating voltage). The cell performance is the worst for $RH_c = 25\%$, better for $RH_c = 50\%$, and the best for $RH_c = 75\%$ with little difference for $RH_c = 100\%$. These changes occur because as the operating voltage increases, the electrochemical reactions slow and only a small amount of liquid water is produced on the cathode side, so cathode flooding is no longer the key factor affecting cell performance. As the water concentration on the cathode side decreases, the mass flow rate of
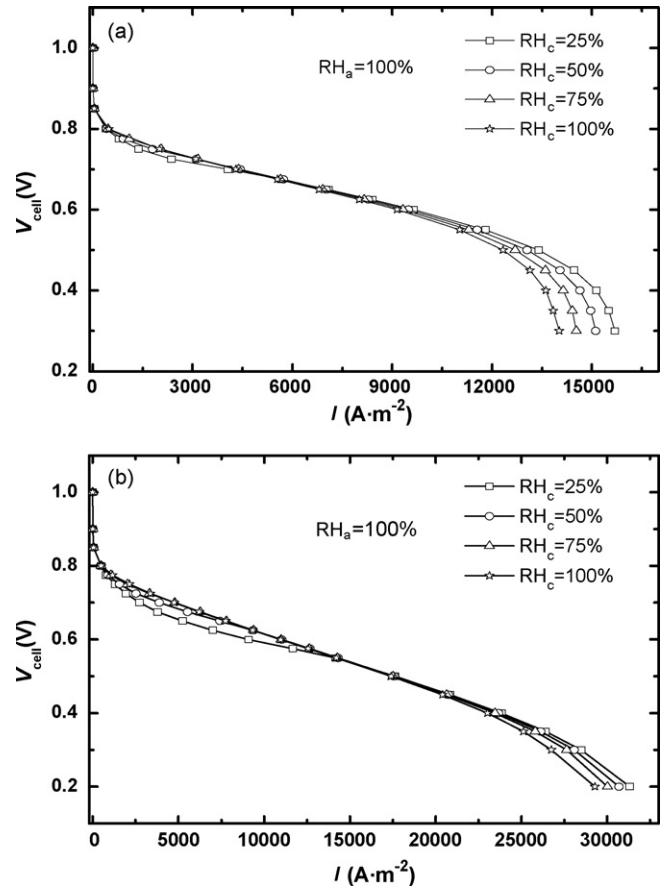

Fig. 5. Effect of cathode relative humidity on the polarization curves: (a) parallel flow field; (b) interdigitated flow field.

water transport from the cathode to the anode by back-diffusion decreases; thus, the membrane hydration gradually becomes the key factor affecting cell performance. Higher RH_c increase the water concentration on the cathode side and the back-diffusion of water, which provides more water for the membrane, resulting in better cell performance. Comparison of Fig. 5(a) and (b) indicates that at the same operating conditions, the flow field design also significantly affects the cell performance. For operating voltages lower than 0.7 V, the interdigitated flow field design has better cell performance than the parallel flow field design. Furthermore, the reversal operating voltages for the parallel and interdigitated flow field designs also differ. For the parallel flow field design, the reversal operating voltage is about 0.7 V, while for the interdigitated flow field design it is about 0.575 V. The baffles at the end of the inlet flow channels in the interdigitated flow field change the reactant transport into the GDL and CL from diffusion to forced convection. This forced convection not only leads to more reactant transport into the GDL and CL for the electrochemical reaction, but also induces larger shear forces which increase liquid water removal. Therefore, the interdigitated flow field design has better performance than the parallel flow field design at low-operating voltages. Additionally, cathode flooding in the interdigitated flow field design is significantly reduced compared with the parallel flow field design, so that the mass flow rate of water from the cathode to the anode by back-
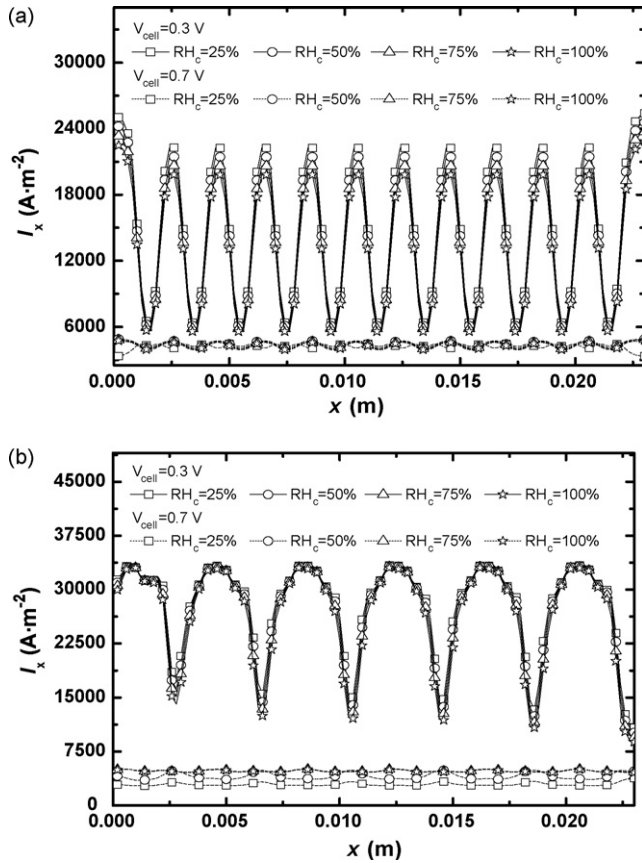
Fig. 6. Effect of cathode relative humidity on the local current densities in the middle cross-section in the PEM at operating voltages of 0.3 and 0.7 V: (a) parallel flow field; (b) interdigitated flow field.
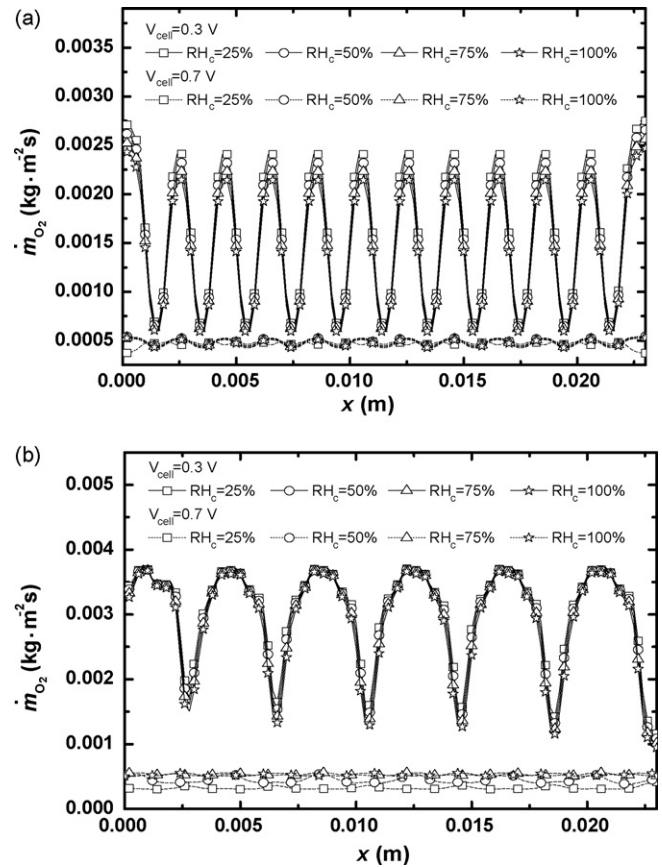

Fig. 7. Effect of cathode relative humidity on the oxygen mass flow rates across the cathode GDL–CL interface at operating voltages of 0.3 and 0.7 V: (a) parallel flow field; (b) interdigitated flow field.

diffusion decreases and the membrane hydration has a more significant effect on cell performance at lower operating voltages than with the parallel flow field design. Thus, the reversal operating voltage for the interdigitated flow field design is lower than for the parallel flow field design.

Fig. 6(a) and (b) show the effect of the cathode relative humidities on the local current densities on the middle cross-section (at $y = 11.5$ mm) in the PEM at operating voltages of 0.3 and 0.7 V for the parallel and interdigitated flow field designs with a constant $RH_a = 100\%$. For the parallel flow field design, the maximum current densities occur at the center of the flow channels with the minimum current densities at the center of the ribs, while for the interdigitated flow field design, the maximum current densities occur at the inlet flow channels with the minimum current densities at the outlet flow channels. At the operating voltage of 0.3 V, for both flow field designs, the minimum and maximum local current densities for $RH_c = 25\%$ are both higher than for the other three cathode relative humidities, so the cell performance is best for $RH_c = 25\%$. However, at the operating voltage of 0.7 V, for both flow field designs, the local current densities for $RH_c = 25\%$ are lower than for the other three cathode relative humidities, so the cell performance is worst for $RH_c = 25\%$.

Fig. 7(a) and (b) show the effect of the cathode relative humidities on the oxygen mass flow rates across the cathode

GDL–CL interface ($y = 11.5$ mm) at operating voltages of 0.3 and 0.7 V for the parallel and interdigitated flow field designs with a constant $RH_a = 100\%$. The oxygen mass flow rate across the GDL–CL interface represents the amount of oxygen entering the CL per unit time; thus, higher oxygen mass flow rates mean that more oxygen participates in the electrochemical reaction in the CL, resulting in larger local current densities. Comparison of Figs. 6 and 7 indicates that the local current densities correlate perfectly with the oxygen mass flow rates, which validates the present model.

Fig. 8(a) and (b) show the effect of the cathode relative humidities on the liquid water concentrations along the cathode GDL–CL interface ($y = 11.5$ mm) at operating voltages of 0.3 and 0.7 V for the parallel and interdigitated flow field designs with a constant $RH_a = 100\%$. For both flow field designs, the liquid water concentrations at the lower operating voltage of 0.3 V are far higher than at the higher operating voltage of 0.7 V, which supports the observation that the mass transport limitation due to cathode flooding is the main factor affecting the cell performance at lower operating voltages. However, at higher operating voltages, the liquid water concentration at the cathode is lower, so concentration polarization has little effect on the cell performance. Although the anode relative humidity is 100%, the mass flow rate of water from the cathode to the anode by back-diffusion decreases at higher operating voltages;
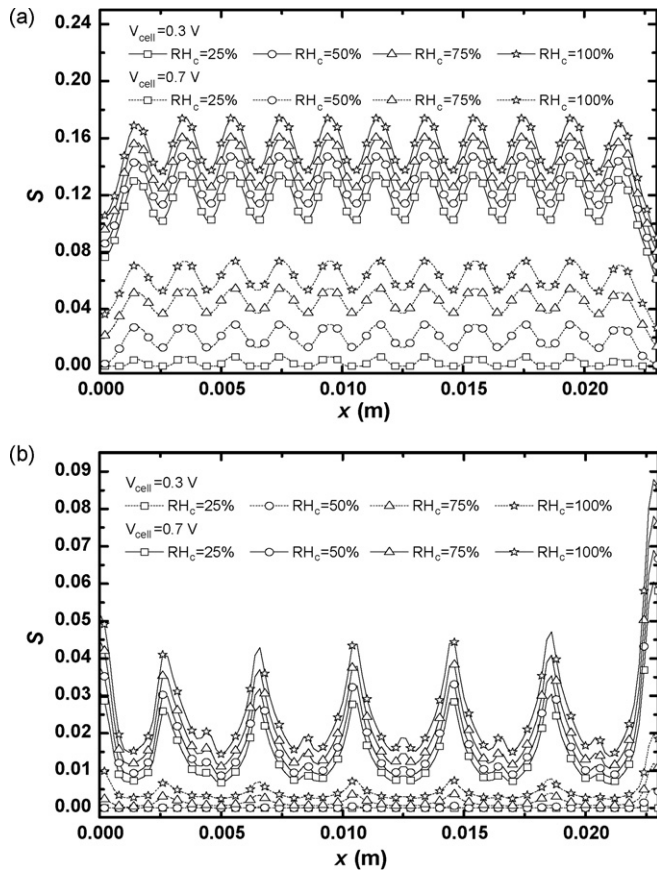
Fig. 8. Effect of cathode relative humidity on the liquid water concentrations along the cathode GDL–CL interface at operating voltages of 0.3 and 0.7 V: (a) parallel flow field; (b) interdigitated flow field.

Fig. 9. Effect of anode relative humidity on the polarization curves: (a) parallel flow field; (b) interdigitated flow field.

thus, the membrane hydration gradually becomes the key factor affecting the cell performance. Fig. 8 shows that at the lower operating voltage of 0.3 V, for both flow field designs, the liquid water concentrations are largest for $RH_c = 100\%$ with the severest concentration polarization, so the cell performance is the worst. Although at the higher operating voltage of 0.7 V, for both flow field designs, the liquid water concentrations are also largest for $RH_c = 100\%$, the concentration polarization is no longer the main factor affecting the cell performance. Higher liquid water concentrations enhance the back-diffusion of water and effectively ensure membrane hydration, which improves cell performance. Comparison of Figs. 7 and 8 shows that the liquid water distributions are exactly reversed from the local oxygen mass flow rate distributions at the lower operating voltage of 0.3 V. For the parallel flow field design, the maximum liquid water concentrations occur at the center of the ribs with the minimums at the center of the flow channels; while for the interdigitated flow field design, the maximum liquid water concentrations occur at the outlet flow channels with the minimums at the inlet flow channels. This occurs because as the liquid water concentrations increase, more pores are blocked in the GDL and CL which increases the oxygen transport resistance, resulting in decreased oxygen mass flow rates. Comparison of Fig. 8(a) and (b) indicates that the liquid water concentrations for the interdigitated flow field design are far less than for the
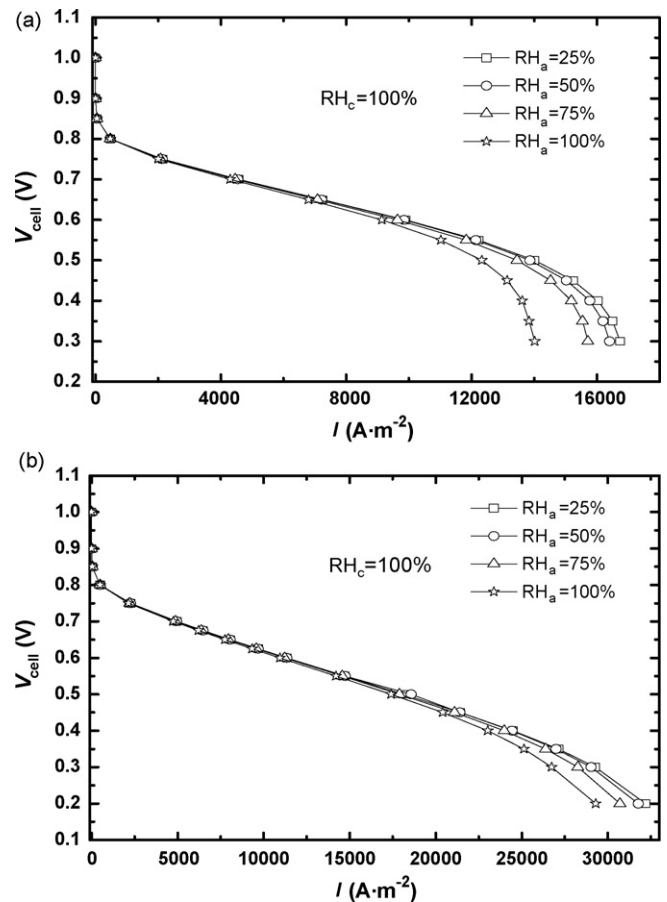
parallel flow field design, which confirms that the interdigitated flow field design has more efficient liquid water removal than the parallel flow field design and significantly reduces cathode flooding. Therefore, as shown in Fig. 5 the concentration polarization in the polarization curves for the interdigitated flow field design is not significant compared to that in the parallel flow field design.

4.2. Effect of anode relative humidity

Fig. 9(a) and (b) show the I–V_{cell} polarization curves for the parallel and interdigitated flow fields at various anode relative humidities with a constant $RH_c = 100\%$. For both flow field designs, at operating voltages greater than 0.7 V, the I–V_{cell} polarization curves for the various RH_a almost coincide, indicating that the cell performance is not dependent on RH_a. However, at operating voltages lower than 0.7 V, the cell performance curves for the various RH_a start to differ. As the RH_a decreases, the limiting current densities increase and the cell performance improves because the molecular weight of hydrogen is far less than that of water, so as the RH_a decreases the hydrogen concentration in the reactants is significantly increased. In addition, at lower operating voltages, the reduced RH_a increases the differences in the water concentrations between the cathode and anode, which not only reduces cathode flooding, but also pro-
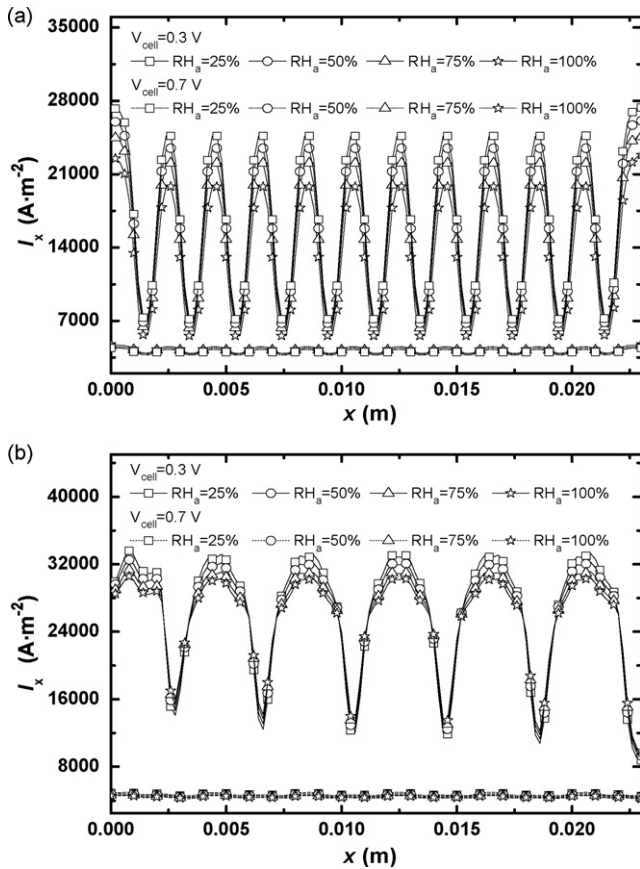
Fig. 10. Effect of anode relative humidity on the local current densities in the middle cross-section in the PEM at operating voltages of 0.3 and 0.7 V: (a) parallel flow field; (b) interdigitated flow field.
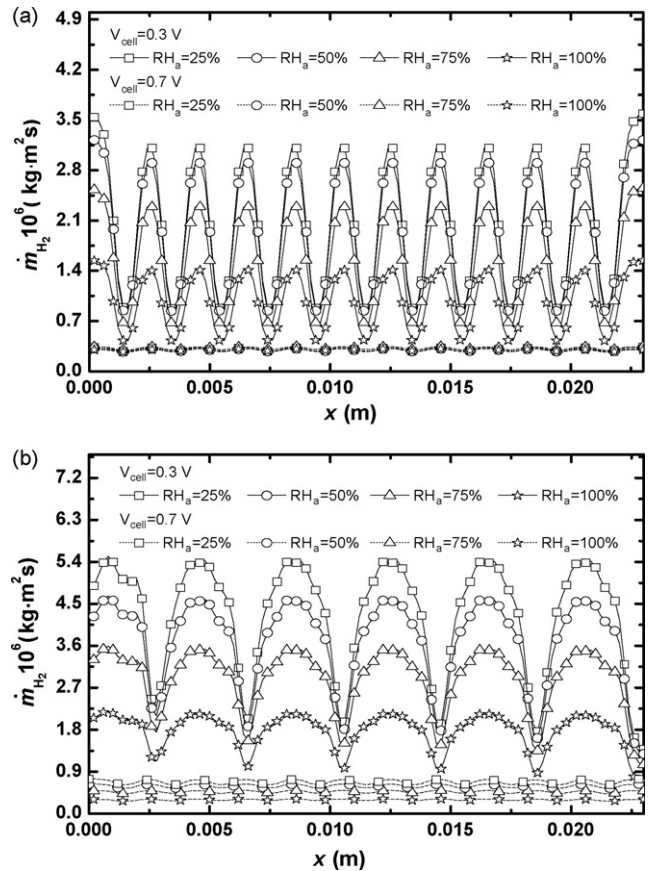

Fig. 11. Effect of anode relative humidity on the hydrogen mass flow rates across the anode GDL–CL interface at operating voltages of 0.3 and 0.7 V: (a) parallel flow field; (b) interdigitated flow field.

vides more water for the membrane, so the cell performance improves.

Fig. 10(a) and (b) show the effect of anode relative humidities on the local current densities on the middle cross-section (at $y = 11.5$ mm) in the PEM at the operating voltages of 0.3 and 0.7 V for the parallel and interdigitated flow field designs with a constant $RH_c = 100\%$. At the operating voltage of 0.7 V, for both flow field designs, the curves of the local current density for various RH_a almost coincide, indicating that the cell performance is not dependent on RH_a. At the operating voltage of 0.3 V, the local current density distributions for the various RH_a are similar to those in Fig. 6 for the various RH_c. For both flow field designs, the local current densities reach maximums at $RH_a = 25\%$, so the cell performance there is best.

Fig. 11(a) and (b) show the effect of the anode relative humidities on the hydrogen mass flow rates across the anode GDL–CL interface ($y = 11.5$ mm) at operating voltages of 0.3 and 0.7 V for the parallel and interdigitated flow field designs with a constant $RH_c = 100\%$. Because a change in the RH_a significantly affects the hydrogen concentration in the reactants, as RH_a decreases the hydrogen mass flow rates significantly increases since there is more hydrogen transport into the CL to participate in the electrochemical reactions which improves cell performance. Fig. 12(a) and (b) show the effect of the anode relative

humidities on the liquid water concentrations along the cathode GDL–CL interface ($y = 11.5$ mm) at operating voltages of 0.3 and 0.7 V for the parallel and interdigitated flow field designs with a constant $RH_c = 100\%$. For both flow field designs, the liquid water concentrations are highest at $RH_a = 100\%$, and as RH_a decreases the liquid water concentrations gradually decrease, indicating that back-diffusion of liquid water from the cathode to the anode increases as the anode relative humidity decreases because the decreasing RH_a increases the differences between the water concentrations at the cathode and anode. Note that previous investigations [34,35,41] indicated that lower anode relative humidities usually resulted in a higher membrane resistance and, thus; higher ohmic voltage losses in the membrane because the cathode relative humidities were maintained at values far less than 100% in those investigations. However, in the present paper, the cathode humidity is maintained at 100%; thus, the high cathode humidity provides sufficient water to maintain membrane hydration by back-diffusion of water. Particularly, at lower operating voltages, the concentration polarization is the main factor affecting the cell performance, with high-liquid water concentrations on the cathode side increasing the oxygen transport resistance. Because a decreasing RH_a reduces cathode flooding, which allows more oxygen to enter the CL to participate in the electrochemical reaction; thus, the cell performance improves.
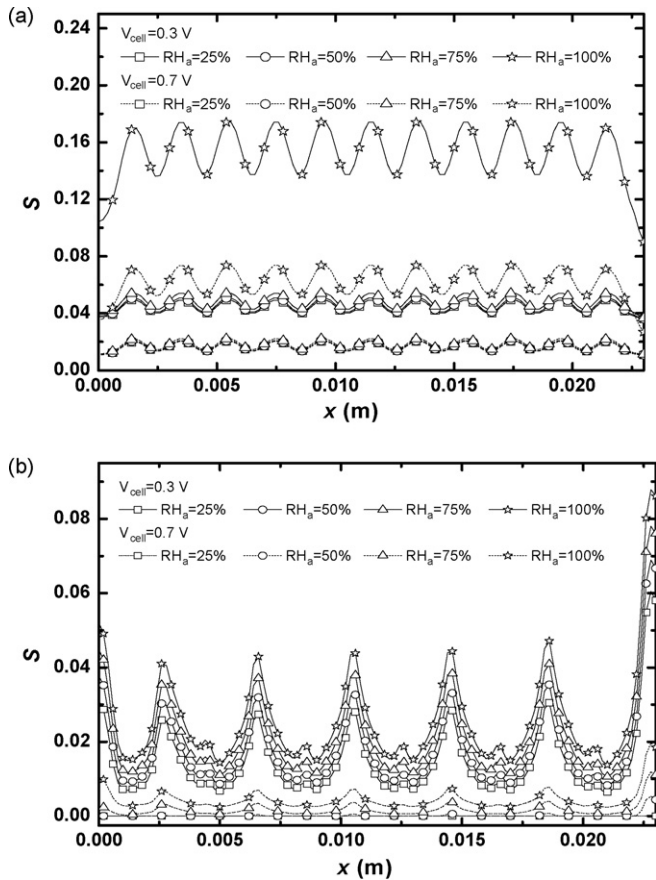
Fig. 12. Effect of anode relative humidity on the liquid water concentrations along the cathode GDL–CL interface at operating voltages of 0.3 and 0.7 V: (a) parallel flow field; (b) interdigitated flow field.

In addition, comparison of Figs. 5 and 9 shows that for the same inlet mass flow rates of reactants on the cathode and anode sides, the reduction of RH_a for a constant $RH_c = 100\%$ is a more effective means for improving cell performance than reducing RH_c with a constant $RH_a = 100\%$. First, both $RH_a = 100\%$ or $RH_c = 100\%$ provide good membrane hydration. Secondly, at lower operating voltages, a large amount of liquid water is produced by the cathode electrochemical reaction with the back-diffusion of water further ensuring membrane hydration. Thus, cathode flooding is the main factor affecting cell performance at lower operating voltages. The reduction of RH_a can lead to more water transport from the cathode to the anode by back-diffusion, which reduces cathode flooding and mass transport losses. Decreasing RH_a also significantly increases the hydrogen concentration in the reactants due to the small molecular weight of hydrogen.

5. Conclusions

The proper relative humidity of the reactants and the proper flow field designs in the bipolar plates both effectively improve water management and cell performance in PEMFC. This paper presented a three-dimensional numerical model based on the finite volume method to analyze the effects of the relative humidities of the reactants on both the cathode and anode sides

on the cell performance for parallel and interdigitated flow fields. The conclusions drawn from the analyses are:

(1) At the same operating conditions and reactant relative humidities, the interdigitated flow field design has better cell performance than the parallel flow field design because the baffle changes the reactant transport into the GDL and CL from diffusion to forced convection, which increases reactant transport rates and enhances liquid water removal.
(2) With a constant $RH_a = 100\%$ for lower operating voltages, a lower RH_c reduces cathode flooding, which improves cell performance. For higher operating voltages, a higher RH_c improves membrane hydration which gives better cell performance.
(3) With a constant $RH_c = 100\%$ for lower operating voltages, a lower RH_a not only provides more hydrogen into the CL to participate in the electrochemical reaction, but also increases the differences between the water concentrations at the anode and cathode, which enhances the back-diffusion of water from the cathode to the anode; thus, reducing the cathode flooding. As a result, a lower RH_a gives better performance than a higher RH_a. For higher operating voltages, the cell performance is not dependent on RH_a.
(4) For the same reactant inlet flow rates on the cathode and anode sides, the reduction of RH_a with a constant $RH_c = 100\%$ is a more effective means to improve cell performance than reducing RH_c with a constant $RH_a = 100\%$.

Acknowledgment

References

[1] J. Larmine, A. Dicks, Fuel Cell Systems Explained, 2nd ed., Wiley, Chichester, West Sussex, 2003.
[2] H. Yang, T.S. Zhao, Q. Ye, J. Power Sources 139 (2005) 79.
[3] X.G. Li, I. Sabir, Int. J. Hydrogen Energy 30 (2005) 359.
[4] T.E. Springer, T.A. Zawodzinski, S. Gottesfeld, J. Electrochem. Soc. 138 (1991) A2334.
[5] D.M. Bernardi, M.W. Verbrugge, AIChE J. 37 (1991) 1151.
[6] D.M. Bernardi, M.W. Verbrugge, J. Electrochem. Soc. 139 (1992) A2477.
[7] T.F. Fuller, J. Newman, J. Electrochem. Soc. 140 (1993) A1218.
[8] T.V. Nguyen, R.E. White, J. Electrochem. Soc. 140 (1993) A2178.
[9] T. Okada, G. Xie, Y. Tanabe, J. Electroanal. Chem. 413 (1996) A49.
[10] V. Gurau, H. Liu, S. Kakac, AIChE J. 44 (1998) 2410.
[11] V. Gurau, F. Barbir, H. Liu, J. Electrochem. Soc. 147 (2000) A2468.
[12] I.S. Yi, T.V. Nguyen, J. Electrochem. Soc. 145 (1998) A1149.
[13] I.M. Hsing, P. Futerko, Chem. Eng. Sci. 55 (2000) 4209.
[14] J.J. Baschuk, X. Li, J. Power Sources 86 (2000) 181.
[15] S. Um, C.Y. Wang, K.S. Chen, J. Electrochem. Soc. 147 (2000) A4485.
[16] N. Djilali, D. Lu, Int. J. Therm. Sci. 41 (2002) 29.
[17] A.A. Kulikovsky, J. Electrochem. Soc. 150 (2003) A1432.
[18] S.H. Ge, B.L. Yi, J. Power Sources 124 (2003) 1.
[19] N.P. Siegel, M.W. Ellis, D.J. Nelson, M.R. von Spakovsky, J. Power Sources 132 (2003) 127.
[20] S. Mazumder, J.V. Cole, J. Electrochem. Soc. 150 (11) (2003) A1503–A1509.
[21] S. Mazumder, J.V. Cole, J. Electrochem. Soc. 150 (11) (2003) A1510–A1517.

[22] W.M. Yan, C.Y. Soong, F. Chen, H.S. Chu, J. Power Sources 125 (2004) 27.
[23] C.Y. Soong, W.M. Yan, C.Y. Tseng, H.C. Liu, F. Chen, J. Power Sources 143 (2005) 36.
[24] W.M. Yan, C.Y. Soong, F. Chen, H.S. Chu, J. Power Sources 143 (2005) 48.
[25] H.C. Liu, W.M. Yan, C.Y. Soong, F. Chen, J. Power Sources 142 (2005) 125.
[26] H.C. Liu, W.M. Yan, C.Y. Soong, F. Chen, H.S. Chu, J. Power Sources 158 (2006) 78.
[27] W.M. Yan, C.H. Yang, C.Y. Soong, F. Chen, M.C. Mei, J. Power Sources 160 (2006) 284.
[28] W.M. Yan, C.Y. Chen, S.C. Mei, C.Y. Soong, F. Chen, J. Power Sources 162 (2006) 1157.
[29] X.D. Wang, Y.Y. Duan, W.M. Yan, J. Power Sources 172 (2007) 265.
[30] X.D. Wang, Y.Y. Duan, W.M. Yan, J. Power Sources 173 (2007) 210.
[31] H.C. Liu, W.M. Yan, X.D. Wang, J. Electrochem. Soc. 154 (12) (2007) B1338.
[32] X.D. Wang, Y.Y. Duan, W.M. Yan, X.F. Peng, J. Power Sources 175 (2008) 397.
[33] C.Y. Wang, Chem. Rev. 104 (2004) 4727.
[34] T.A. Zawodziniski, T.E. Springer, F. Uribe, S. Gottesfeld, Solid Stage Ionics 60 (1993) 199.
[35] M. Cappadonia, J.W. Erning, S.M.S. Niaki, U. Stimming, Solid Stage Ionics 77 (1995) 65.
[36] N. Rajalakshmi, P. Sridhar, K.S. Dhathathreyan, J. Power Sources 109 (2002) 452.
[37] S. Yoshioka, A. Yoshimura, H. Fukumoto, O. Hiroi, H. Yoshiyasu, J. Power Sources 144 (2005) 146.
[38] G. Lin, W. He, T.V. Nguyen, J. Electrochem. Soc. 151 (12) (2004) A1999.
[39] D. Natarajan, T.V. Nguyen, J. Power Sources 115 (2003) 66.
[40] Y. Yoshikawa, T. Matsuura, M. Kato, M. Hori, J. Power Sources 158 (2006) 143.
[41] M. Amirinejad, S. Rowshanzamir, M.H. Eikani, J. Power Sources 161 (2006) 872.
[42] J.H. Jang, W.M. Yan, H.Y. Li, Y.C. Chou, J. Power Sources 159 (2006) 468.
[43] C. Lee, H.S. Chu, J. Power Sources 161 (2006) 949.
[44] W. He, Yi FJ.S., T.V. Nguyen, AIChE J. 46 (2000) 2053.
[45] F.A.L. Dullien, Porous Media, Academic Press, New York, 1991.
[46] S.V. Patankar, Numerical Heat Transfer and Fluid Flow, Hemisphere/McGraw-Hill, New York, 1980.
[47] C.H. Cheng, Development of Shape Designer for the Flow Channels of Bipolar Plate for PEM Fuel Cells (2/3), Technical Report of NSC-93-2212-E-036-001, National Science Council, Taiwan, 2004.